Nature Environment and Pollution Technology
An International Quarterly Peer-Reviewed Open Access Journal

p-ISSN: 0972-6268 | e-ISSN: 2395-3454 Vol. 25 | No. 4 | Article ID B4422 | 2026

RESEARCH ARTICLE https://doi.org/10.46488/NEPT.2026.v25i04.B4422 OPEN ACCESS

Eco-Friendly Degradation of Textile Azo Dye Reactive Orange ME2RL Using *Pseudomonas stutzeri*-Mediated Iron Oxide Nanoparticles

P. Zambare[1,2,4], S. Kanase[1,2,4] and A. Raut[3,4]†
[1]Rayat Institute of Research and Development, Satara, 415001, Maharashtra, India
[2]Department of Microbiology, Yashavantrao Chavan Institute of Science, Satara, 415001, Maharashtra, India
[3]Department of Microbiology, Yashwantrao Chavan College of Science, Karad, 415110, Maharashtra, India
[4]Department of Microbiology, Shivaji University, Kolhapur, 416004, Maharashtra, India
†Corresponding author: A. Raut; rautavinash@gmail.com

ARTICLE HISTORY

Received: 18-12-2025
Revised: 15-03-2026
Accepted: 18-03-2026

KEYWORDS

Pseudomonas stutzeri
Reactive orange ME2RL
Iron oxide
Nanoparticles
Biophysical analysis

CITE THIS ARTICLE

Zambare, P., Kanase, S., and Raut, A., 2026. Eco-friendly degradation of textile azo dye reactive orange ME2RL using *Pseudomonas stutzeri*-mediated iron oxide nanoparticles. *Nature Environment and Pollution Technology*, 25(4), B4422. https://doi.org/10.46488/NEPT.2026.v25i04.B4422

PUBLISHED BY

TECHNOSCIENCE PUBLICATIONS

ABSTRACT

The discharge of synthetic azo dyes from textile industries poses serious environmental and health risks because of their genotoxic, mutagenic, and carcinogenic nature. In the present study, eco-friendly iron oxide (Fe_2O_3) nanoparticles were biosynthesized using *Pseudomonas stutzeri* and ferric chloride as a precursor under ambient conditions and were applied for the degradation of the textile dye Reactive Orange ME2RL. The synthesized nanoparticles were characterized using UV–Visible spectroscopy, FTIR, SEM, HRTEM, and DLS, confirming the formation of stable nanoscale Fe_2O_3 particles. The nanoparticles exhibited efficient catalytic activity, achieving nearly 80% degradation of Reactive Orange ME2RL within 45 min. The degradation pathway and the formation of intermediate metabolites were confirmed using UV–Visible spectroscopy, FTIR, HPLC, and GC–MS analyses. Furthermore, phytotoxicity and fish toxicity assays indicated reduced toxicity of the degradation products. These results demonstrate that biosynthesized Fe_2O_3 nanoparticles offer a rapid, efficient, and environmentally sustainable approach for the remediation of azo dye-contaminated textile wastewater.

1. INTRODUCTION

Textile sectors occupy a significant position in the Indian economy by contributing to industrial production, exports, and employment (Chavan 2001). However, the use of synthetic dyes has made textile effluents a persistent source of environmental pollution because of their adverse effects on the environment and living organisms (Banat et al. 1997). Textile wastewater is typically characterized by intense color, high chemical oxygen demand (COD), high total dissolved solids (TDS), and the presence of recalcitrant aromatic compounds, making conventional treatment highly challenging. The persistence of these dyes in aquatic ecosystems reduces light penetration, inhibits photosynthesis, and contributes to long-term ecological imbalance (Patel & Bhatt 2022, Haroon et al. 2023).

Scientists are increasingly interested in metal nanoparticles because of their remarkable chemical, electrical, and optical properties. The green synthesis of such nanoparticles is simple, environmentally friendly, and provides a rapid approach to meeting the growing global demand for safe, non-toxic, and biocompatible nanoparticles (Khan et al. 2019). Researchers have shown particular interest in the green synthesis of nanoparticles using microbes because of their ease of handling,

environmentally safe disposal, and relatively simple downstream processing (Annamalai et al. 2021). Among microorganisms, bacteria possess the innate ability to reduce metal ions and synthesize metal nanoparticles (Srivastava & Constanti 2012). Microbial synthesis not only avoids the use of toxic reducing agents employed in conventional chemical methods but also enables precise control over nanoparticle morphology through enzymatic and metabolic pathways. Consequently, microbial nanotechnology has emerged as a promising tool for sustainable environmental remediation (Annamalai et al. 2021).

Because of their genetic diversity and adaptable metabolic systems, microorganisms are considered a preferred choice for the biological remediation of dye pollution (Banat et al. 1997, Shakoor et al. 2025). In addition, biological treatment requires fewer reagents and produces less sludge than many physicochemical methods, making it a more economical and environmentally friendly alternative. It can also result in the complete mineralization of dyes and is considered a cost-effective treatment strategy (Pandey et al. 2007). Iron nanoparticles (FeNPs) have shown considerable potential for reducing environmental pollution.

The phylum Proteobacteria includes *Pseudomonas stutzeri*, which is classified under group I of Palleroni's DNA–rRNA homology groups (Palleroni et al. 1973, Palleroni 1984). It is currently recognized as a member of the class Gammaproteobacteria. *P. stutzeri* is a widely distributed, non-fluorescent denitrifying bacterium that has also been identified as an opportunistic human pathogen (Rossello et al. 1991). Over the past few decades, the taxonomy of this diverse species has been clarified, and its unique metabolic properties have attracted considerable attention. Some strains are capable of fixing dinitrogen and have served as model organisms for studies on denitrification. Other strains degrade environmental contaminants or interact with toxic metals, while several exhibit natural transformation capabilities, making them valuable for studies of environmental gene transfer (Palleroni et al. 1970). Importantly, *P. stutzeri* has been reported to tolerate and transform a wide range of xenobiotics, making it a promising candidate for bio-nanotechnological applications, including microbial nanoparticle synthesis and dye biodegradation (Shahriarinour et al. 2021).

The textile, food, leather, cosmetic, plastic, and paper industries use a wide variety of organic dyes for aesthetic purposes, many of which are hazardous and pose serious environmental threats (Forgacs et al. 2004). The treatment and removal of organic dyes from textile effluents remain major challenges for both industry and environmental scientists. Although several physicochemical techniques are available, they are often inefficient and may generate secondary pollutants that require additional treatment. Techniques such as ozonation, coagulation-flocculation, adsorption, and membrane filtration may achieve partial color removal but frequently fail to completely degrade dye molecules, resulting in secondary pollution and high operational costs (Periyasamy 2024).

In recent years, interest in advanced nanocatalyst-based technologies for the removal of dyes and other organic pollutants has increased significantly (Naz et al. 2021). A simple and sustainable approach involves treating dyes in the presence of biocompatible and environmentally safe catalysts without the use of organic solvents. Reactive Orange ME2RL is a diazo dye widely used in the textile industry for coloring wool, silk, leather, paper, and polyamide fibers. Considerable attention has been directed towards the degradation of this dye because its complex aromatic backbone and multiple azo linkages make it resistant to conventional biological degradation, highlighting the need for integrated nano-biotechnological approaches for efficient treatment (Joshi et al. 2015).

In this study, *Pseudomonas stutzeri*, a bacterium known for degrading diazo dyes containing two –N=N– azo bonds (Joshi et al. 2020), was evaluated for its bioremediation potential. The biodegradation of the common textile diazo dye Reactive Orange ME2RL was investigated using iron nanoparticles synthesized by an isolated strain of *Pseudomonas stutzeri*. The combined application of microbially synthesized FeNPs and dye-degrading bacteria provides a synergistic strategy that enhances both catalytic activity and biodegradation efficiency, thereby offering a sustainable, cost-effective, and environmentally friendly approach for treating textile effluents.

In the present study, we focused on the degradation of the textile dye Reactive Orange ME2RL using Fe□O□ nanoparticles synthesized by *Pseudomonas stutzeri*. Reactive Orange ME2RL is known to damage the eyes, mucous membranes, and upper respiratory tract and has also been reported to be carcinogenic (Gupta et al. 2006). In addition, it increases biological oxygen demand by reducing light penetration and oxygen availability in aquatic ecosystems, thereby adversely affecting aquatic life. Therefore, this dye should be removed from wastewater before its discharge into natural water bodies because of its harmful effects on human health and its long-term environmental impacts (Ali 2010).

2. MATERIALS AND METHODS

2.1. Materials

The nutrient agar, 99% pure $FeCl_3$, and nutrient broth used

in this study were all sourced from Himedia Laboratories Pvt. Ltd., an Indian company. Materials such as Reactive Orange ME2RL, ethyl acetate, $FeCl_3$, and methanol were obtained from Sigma-Aldrich in India. All ingredients were of analytical reagent grade.

2.2. Methods

2.2.1. Iron Nanoparticle Biosynthesis

The bacterial strain *Pseudomonas stutzeri* was isolated from a soil sample collected at Kaas Pathar in Satara, Maharashtra, India. Its molecular identification was conducted via 16S rRNA sequencing at NCMR, Pune (Mukherjee & Dutta 2019). The pure culture was inoculated into sterile nutrient broth and incubated at 28°C for 24 h with shaking at 120 rpm. After harvesting and washing the bacterial biomass, it was suspended in sterile distilled water and agitated at 120 rpm for 24 h at 28°C. The cell-free extract (CFE), obtained after centrifugation, was used for nanoparticle synthesis. To initiate nanoparticle formation, 1 mM $FeCl_3$ was added to the CFE in an equal volume, and the mixture was stirred at 120 rpm at 28°C. A control sample consisted of 1 mM $FeCl_3$ solution without CFE. The formation of iron nanoparticles was monitored visually and by UV–visible spectroscopy at regular intervals. The capacity of *P. stutzeri* to synthesize iron nanoparticles aligns with previous reports of microbial nanoparticle production by Pseudomonas spp. (Vasantharaj et al. 2019).

2.2.2. Characterization of Iron Nanoparticles

The excitation spectra of biosynthesized iron nanoparticles were recorded using a UV–Visible spectrophotometer (Systronics AU-270I) (Velusamy et al. 2016). Crystallinity was analyzed by X-ray diffraction (XRD, Bruker D8 Advance) within a 2θ range of 20°–80°, operating at 40 kV and 40 mA (Giuli et al. 2015). XRD is a common technique to determine the crystal structure and phase composition of nanoparticles (Holzwarth & Gibson 2011). Scanning electron microscopy (SEM) was employed to observe the morphology of the iron nanoparticles. High-resolution transmission electron microscopy (HRTEM) using an FEI Tecnai G2 U-Twin provided data on particle size and shape. Dynamic light scattering (DLS) analysis with a Nicomp 388 ZLS system assessed the hydrodynamic size distribution (Chicea et al. 2012). Fourier transform infrared (FTIR) spectroscopy (Shimadzu FTIR-8400), covering 400–4000 cm^{-1}, was conducted to identify biomolecules involved in nanoparticle reduction and stabilization (Zhao et al. 2016).

2.2.3. Degradation of Reactive Orange ME2RL Using Iron Nanoparticles

The catalytic degradation capacity of biosynthesized iron nanoparticles was assessed using Reactive Orange ME2RL dye. A 1 mM concentration of FeNPs was added to 100 mL of dye solution (10 mg L^{-1}), and the mixture was stirred at 120 rpm for 30 min (Al-Musawi et al. 2022). At regular intervals, 2 mL samples were taken, and their absorbance at 494 nm was measured to determine the degradation percentage using Equation 1.

$$\text{Degradation (\%)} = \frac{D_0 - D_1}{D_0} \times 100 \quad \ldots(1)$$

Where,

D_0 = initial absorbance

D_1 = final absorbance

2.3. Study of Metabolites of the Degraded Dye

2.3.1. UV–Visible Spectroscopy

The spectral changes of control and treated dye samples (400–800 nm) were analyzed to confirm biodegradation rather than superficial decolorization (Wu et al. 2022).

2.3.2. Fourier Transform Infrared Spectroscopy (FTIR)

FTIR analysis was performed to understand functional group alterations during degradation and nanoparticle interaction (Katata-Seru et al. 2018).

2.3.3. High-Performance Liquid Chromatography (HPLC)

HPLC analysis was conducted using a C18 column (4.6 × 250 mm) with methanol as the mobile phase at a flow rate of 1 mL min^{-1}. A UV detector monitored dye metabolites at their maximum absorption wavelengths (Ferreira et al. 2020). Supernatants from degradation experiments (0–45 min) were analyzed, with metabolites extracted using ethyl acetate, dried over anhydrous Na_2SO_4, evaporated, and reconstituted in HPLC-grade methanol (Apine et al. 2023).

2.3.4. Gas Chromatography–Mass Spectrometry (GC–MS)

Extracted metabolites were subjected to GC–MS analysis after solvent evaporation and reconstitution. This process followed standard extraction protocols for dye degradation metabolites (Castro et al. 2020).

2.3.5. Antibacterial Activity of Iron Nanoparticles

The antibacterial properties of FeNPs were evaluated using the agar well diffusion method. Test organisms included *Proteus vulgaris* (NCIM-2813), *Salmonella typhi* (NCIM-2501), *Staphylococcus aureus* (NCIM-2654), and *Pseudomonas aeruginosa* (NCIM-5032). Solutions of antibiotics, FeNPs, and their combinations were placed into agar wells and incubated at 37°C for 24 h. The zones of inhibition were measured in millimeters, and the percentage increase in antibacterial activity was calculated using Equation 2 (Mane et al. 2008).

$$\text{Percent Fold Increase} = \frac{B-A}{A} \quad \ldots(2)$$

Where

A = inhibition zone of antibiotic

B = inhibition zone of antibiotic + FeNPs

2.4. Phytotoxicity Studies

The phytotoxic effects of the parent dye and its degradation metabolites were evaluated on four types of agricultural seeds: *Vigna radiata* (green gram), *Triticum aestivum* (wheat), *Vigna unguiculata* (cowpea), and *Pisum sativum* (pea). Seeds were exposed to dye and metabolite solutions at concentrations up to 400 ppm, following published protocols (Aly et al. 2025). Distilled water was used as a control. After seven days, parameters such as germination rate and plumule and radicle lengths were measured as described previously (Ameur et al. 2012).

2.5. Fish Toxicity Studies

Glass aquaria were sterilized with 0.1% potassium permanganate to prevent fungal contamination (Hanafi & Sapawe 2020). Fish were acclimated before being exposed to different concentrations of Reactive Orange ME2RL dye. The LC_{50} values were calculated after 96 h of exposure. Histological examinations were performed on the treated fish to evaluate tissue alterations (Islam et al. 2021).

2.6. Determination of LC_{50} and Percent Mortality

A straightforward method for assessing a substance's toxicity is through LC_{50} determination. Well-acclimated fish from the stock were divided into seven groups, each consisting of ten healthy individuals representing different dye treatments. These groups were then transferred to glass aquariums containing varying dye concentrations (1.25, 2.5, 3.75, 5.00, 6.25, 7.5, and 8.75 ppm). The fish were exposed to their respective concentrations for a specified duration, and mortality was recorded over 96 h. Dead fish were counted at 24, 48, 72, and 96 h for each concentration. To ensure accuracy, the experiments were repeated three times to confirm the mortality rates and determine the LC_{50} value (Islam et al. 2021). Mortality percentages were calculated using the following formula:

$$\%\ \text{Mortality} = \frac{\text{Number of dead fish}}{\text{Initial number of stocked fish}} \times 100 \quad \ldots(3)$$

3. RESULTS AND DISCUSSION

3.1. Overview

In the present study, the bacterial strain *Pseudomonas stutzeri* was employed for the biosynthesis of iron nanoparticles. These biosynthesized nanoparticles exhibited remarkable catalytic efficiency in degrading Reactive Orange ME2RL. The rapid degradation underscored the enhanced reactivity and surface properties conferred by the green synthesis approach. Instrumental analysis confirmed the conversion of the parent azo dye into less complex, non-toxic metabolites, demonstrating complete breakdown of chromophoric groups. Beyond dye degradation, the nanoparticles also demonstrated excellent antibacterial activity against pathogenic bacterial strains, with an additive effect observed when combined with conventional antibiotics. Toxicity assays on phytotoxicity and fish toxicity confirmed that the degradation products were non-toxic, supporting the environmental safety of the process. Overall, the combined characterization, catalytic performance, and toxicity assessments highlight the potential of *Pseudomonas stutzeri*-derived iron nanoparticles as an efficient, eco-friendly solution for textile dye bioremediation.

3.1.1. Biosynthesis of Iron Nanoparticles

The biosynthesis of iron nanoparticles (Fe NPs) using isolated *Pseudomonas stutzeri* was confirmed by visual changes that occurred during the bioreduction of ferric ions.

Upon adding $FeCl_3$ solution to CFE, the reaction mixture gradually changed color from pale yellow to a distinct reddish-brown within 24 h, further intensifying over the next 48 h (Fig. 1). This color transition was caused by NADH-dependent reductases that drove the redox process, while proteins and polysaccharides acted as capping agents by binding to nanoparticle surfaces through functional groups such as amide, hydroxyl, and carboxyl (Acharya et al. 2025). This chromatic shift is a recognized marker of nanoparticle formation and is attributed to surface plasmon resonance (SPR) excitation, which occurs when iron nuclei nucleate and cluster at the nanoscale (Jana et al. 2016).

3.2. Characterization of Nanoparticles

3.2.1. UV-Visible Spectroscopy

Fig. 1: (a) Cell-free extract; (b) color change after addition of precursor ($FeCl_3$) solution.

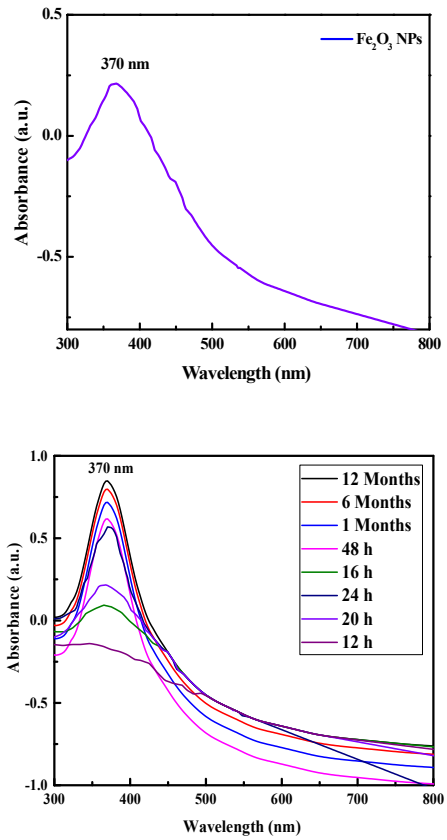

Fig. 2: UV spectrum of iron nanoparticles synthesized by Pseudomonas stutzeri.

Apart from visual confirmation, UV spectroscopy further validated the biosynthesis of the nanoparticles by sensitively monitoring nucleation and growth processes in metal nanostructures. The initial CFE showed no significant absorbance in the visible spectrum, confirming the absence of pre-existing nanoparticles. Upon addition of $FeCl_3$, a distinct absorption band appeared at 370 nm, corresponding to the characteristic surface plasmon resonance of biogenic iron nanoparticles (Fig. 2). The presence of the 370 nm peak aligns with previous studies on microbial and plant-based iron nanoparticles, validating successful synthesis under ambient conditions (Ganachari et al. 2012, Nurbas et al. 2017). Variations in peak sharpness and intensity provide mechanistic insights: the moderate bandwidth suggests a relatively narrow size distribution, supported by TEM and DLS results. The stability of the peak without significant red-shifting implies controlled growth and effective capping by biomolecules in the CFE, which prevent particle aggregation. Overall, UV–visible analysis not only confirms nanoparticle formation but also offers insights into the kinetics and stabilization mechanisms of biogenic synthesis, demonstrating the efficiency of *P. stutzeri*-mediated Fe nanoparticle production.

The stability of the synthesized Fe_2O_3 nanoparticles was assessed by tracking their UV–visible absorption spectra over a span of 12 h to 12 months (Fig. 2). The consistent spectral profile indicates that the Fe_2O_3 nanoparticles maintain their structural and optical integrity for up to 12 months under storage conditions, demonstrating excellent colloidal stability.

3.2.2. FTIR

FTIR measurements of iron nanoparticles helped to reveal information about chemical changes in functional groups complexed in the reduction process of iron ions to iron nanoparticles (Giuli et al. 2015).

Fig. 3 displays five distinct peaks at 3344 cm^{-1}, 2925 cm^{-1}, 1631 cm^{-1}, 1022 cm^{-1}, and 538 cm^{-1}, characteristic of Fe_2O_3 NPs. These peaks correspond to the asymmetric stretching of C–H bonds, C–O stretching, and O–H stretching vibrations (alcoholic or phenolic), indicating the presence of functional groups that play a key role in stabilizing and capping the iron nanoparticles. The emergence of a new peak at 538 cm^{-1} confirms the formation of Fe–O bonds, demonstrating successful synthesis and biomolecular capping.

3.2.3. XRD

To gain a deeper understanding of the formation and crystallinity of the synthesized iron nanoparticles, XRD analysis was performed (Holzwarth & Gibson 2011). The XRD pattern, illustrated in Fig. 4, displays prominent diffraction peaks at 31.94°, 45.5°, 56.6°, 66.33°, and 75.38°, corresponding to the crystal planes 220, 400, 511, 440,

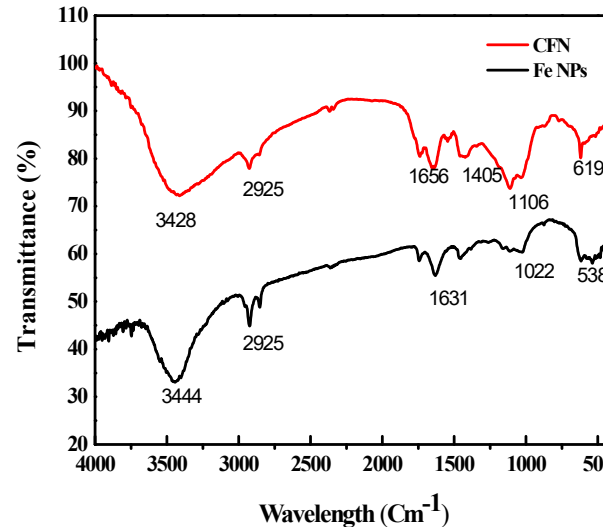

Fig. 3: FTIR of iron nanoparticles.

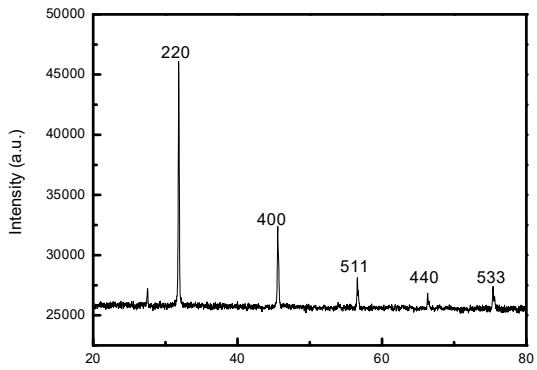

Fig. 4: XRD pattern of iron nanoparticles.

and 533, respectively. The peaks are closely aligned with γ-Fe_2O_3, consistent with JCPDS card 39-1346. The strong diffraction peaks confirm the crystalline structure and phase of the iron nanoparticles, indicating the formation of Fe_2O_3 nanoparticles. The estimated nanoparticle size, calculated using the Debye–Scherrer equation, is approximately 32 nm, suggesting a high surface area–to–volume ratio. The crystallite size was determined employing the Debye–Scherrer formula (Chicea et al. 2012).

3.2.4. DLS

DLS was used to analyze the particle size distribution of the synthesized nanoparticles (Javidparvar et al. 2016). The particle size distribution revealed the hydrodynamic size of the nanoparticles. Most particles ranged from 50 to 100 nm, with an average particle size of 50 nm (Fig. 5). The hydrodynamic size closely resembled the particle size determined by SEM analysis, although DLS often reports larger particle sizes because of agglomeration. The DLS analysis showed that the iron nanoparticles had particle sizes ranging from 50 to 100 nm. The hydrodynamic size includes both the metallic core and the coating material.

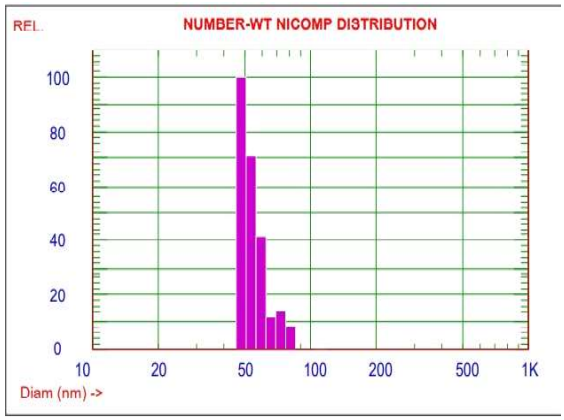

Fig. 5: Hydrodynamic particle size measurement using the DLS (volume-weighted) method.

DLS measures the hydrodynamic diameter of nanoparticles dispersed in a liquid medium, which includes not only the nanoparticle core but also the surrounding solvation layer, surface-bound biomolecules, and possible agglomeration in the suspension. Consequently, the measured particle size appears larger (Bhattacharjee 2016).

3.2.5. SEM

Surface morphology of iron nanoparticles was examined using SEM (Saha & Bhunia 2020), as illustrated in Fig. 6. The SEM images revealed monodispersed FeNPs ranging from 20 to 50 nm in size. The particles exhibited smooth surfaces and a high degree of crystallinity. The micrographs displayed well-defined borders, with an average particle size of 33 nm.

3.2.6. HRTEM

The optimized nanoparticles' size and morphology were examined using HRTEM, confirming the presence of nearly spherical iron nanoparticles (Fig. 7). Their sizes range from approximately 20 to 50 nm. Similar results have been documented in previous research (Katata-Seru et al. 2018, Sekar et al. 2012).

3.3. Catalytic Degradation of Reactive Orange ME2RL Using Biogenic Iron Nanoparticles

Upon adding iron nanoparticles (10 mg L^{-1}) to the dye solution, a gradual degradation occurred under visible light. The solution's color shifted from orange to colorless within 45 min (Fig. 8). These results align with previous reports (Joshi et al. 2015).

The characteristic absorption peak at 494 nm was used to assess the catalytic activity of iron nanoparticles. The reduction process was evidenced by a consistent decrease in the maximum absorbance (kmax) at 494 nm, with minimal shifts in λmax. The peak at 494 nm diminished over 45 min, indicating that Reactive Orange ME2RL was undergoing

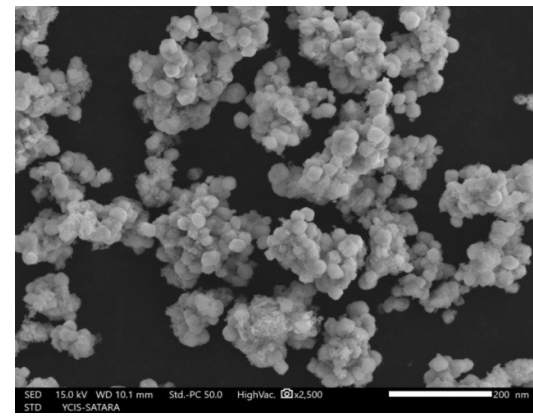

Fig. 6: SEM images of iron nanoparticles.

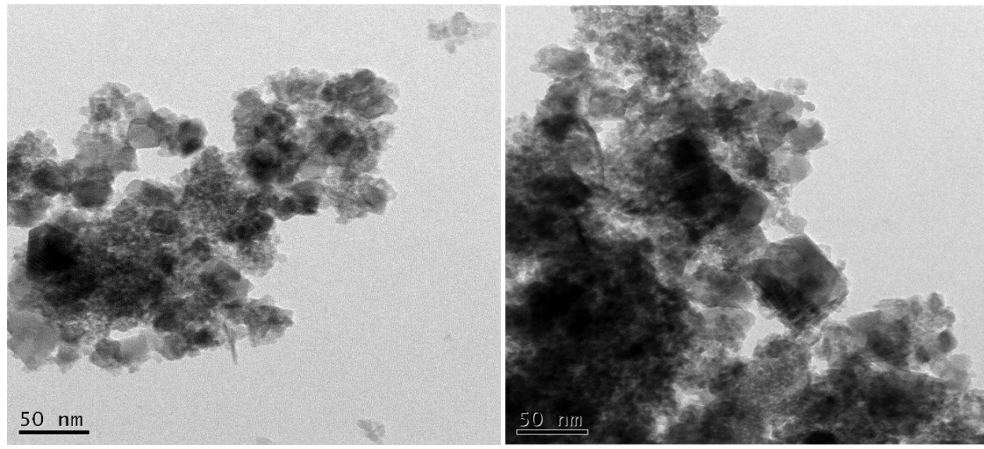

Fig. 7: HRTEM images of iron nanoparticles.

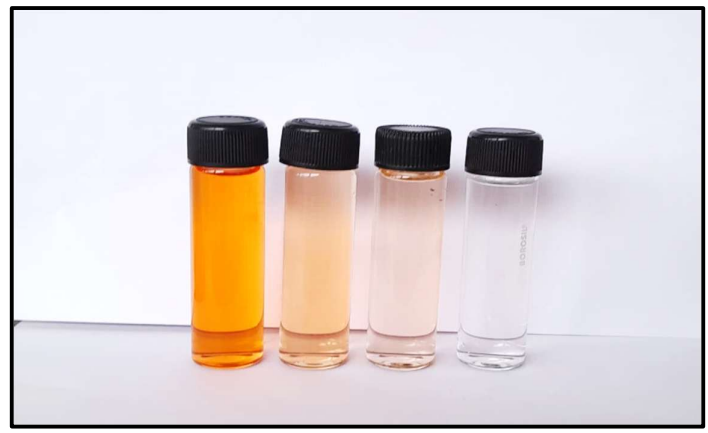

Fig. 8: Gradual color changes from orange to colorless after the addition of iron.

degradation (Fig. 9). Additionally, small peaks and a broad band between 600–750 nm suggested the formation of intermediate by-products (Forgacs et al. 2004).

The degradation experiments were conducted under ambient laboratory lighting conditions, which suggests that the observed dye removal may be partly due to the photocatalytic activity of Fe_2O_3 nanoparticles. During photodegradation, the formation of highly reactive hydroxyl radicals (•OH) is triggered by the generation of electron–hole (e^-/h^+) pairs on the surface of the photoactivated catalyst. As shown in Fig. 10, a simplified mechanism illustrates how free radicals (•OH) are formed and how they facilitate the photocatalytic breakdown of Orange ME2RL dye. When exposed to light, electrons are excited from the valence band to the conduction band, creating electron–hole pairs (Eq. (4)). The electrons in the conduction band can then migrate to the hematite surface, reducing Fe^{3+} ions (Eq. (5)), or react with hydrogen peroxide molecules to produce reactive radical species (Eq. (6)). Concurrently, the generated holes react with surface-adsorbed water (Eq. (7)) and HO^- ions (Eq. (8)). Additionally, Fe^{2+} on the surface can be oxidized back to Fe^{3+} in the presence of adsorbed H_2O_2 (Eq. (9)), which further promotes the formation of •OH radicals. These radicals are the primary oxidants responsible for degrading the dye, as supported by existing studies (Vu et al. 2019, Huang et al. 2015).

$$Fe_2O_3 + hv \rightarrow e^- + h^+ \quad ...(4)$$

$$Fe_2O_3 + e^- \rightarrow Fe^{2+} \quad ...(5)$$

$$e^- + H_2O_2 \rightarrow \bullet OH + HO^- \quad ...(6)$$

$$h^+ + H_2O \rightarrow H^+ + \bullet OH \quad ...(7)$$

$$HO^- + h^+ \rightarrow \bullet OH + H^+ \quad ...(8)$$

$$Fe^{2+} + H_2O_2 \rightarrow Fe^{3+} + \bullet OH + HO^- \quad ...(9)$$

Additionally, it is important to consider that •OH radicals can be formed by direct photolysis as follows:

$$H_2O_2 + hv \rightarrow 2\ \bullet OH \quad ...(10)$$

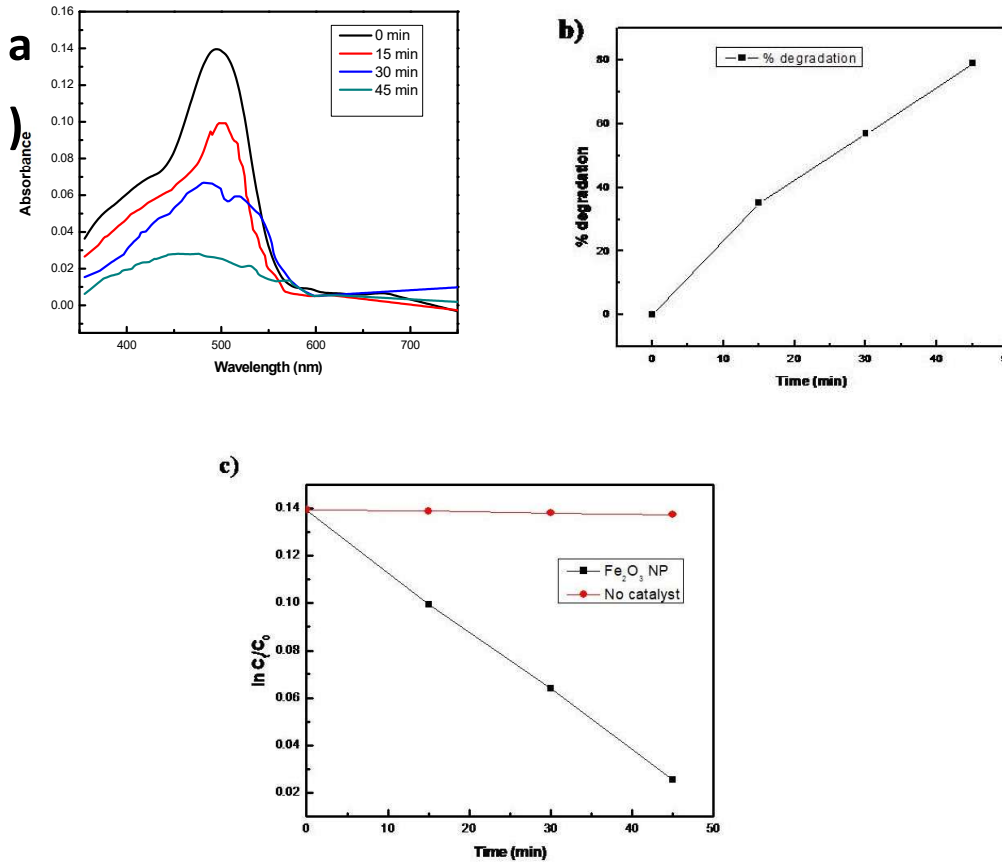

Fig. 9: (a) UV–visible absorption spectra of Orange ME2RL dye using Fe_2O_3 nanoparticles at various time intervals; (b) degradation (%) of Orange ME2RL dye with time in the presence of Fe_2O_3 nanomaterial; (c) $\ln(C_t/C_0)$ versus degradation time plot for finding the reaction rate constant (kapp).

The degradation experiments were performed at an initial dye concentration of 10 mg L^{-1} to assess the fundamental catalytic performance of the biosynthesized Fe_2O_3 nanoparticles under controlled laboratory conditions. In practical scenarios, such as textile effluents, dye concentrations often exceed 100 mg L^{-1}, which may lead to reduced degradation efficiency due to saturation of active catalytic sites and mass transfer limitations. Therefore, additional studies at higher dye concentrations are necessary to evaluate the system's real-world applicability. Figs. 9(a), 9(b), and 9(c) illustrate the degradation kinetics of Reactive Orange ME2RL in the presence of biosynthesized Fe_2O_3, analyzed using a pseudo-first-order model. Kinetic analysis involved plotting $\ln(C_t/C_0)$ against reaction time, where C_0

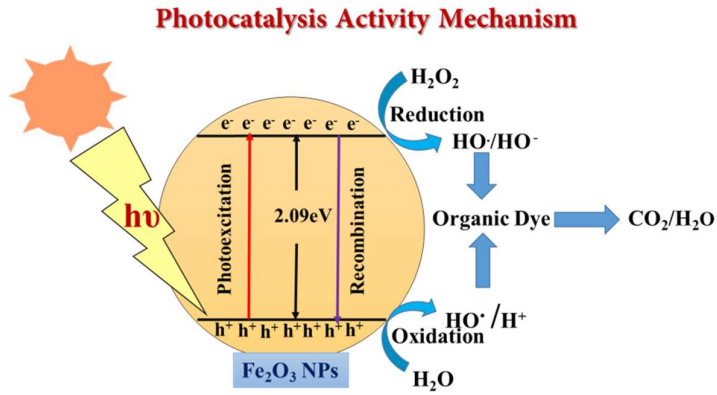

Fig. 10: Photodegradation mechanism of Orange ME2RL dye in the presence of Fe_2O_3 nanoparticles.

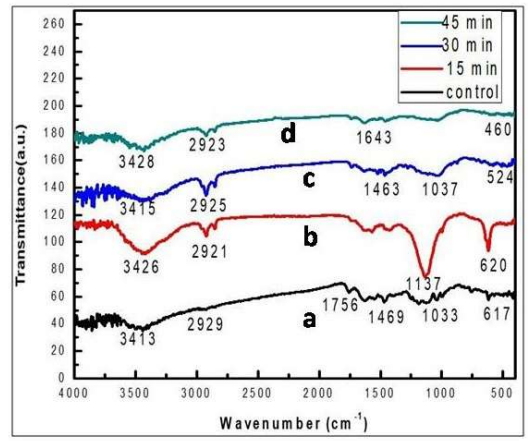

Fig. 11: FTIR of Orange ME2RL dye upon degradation: (a) pure dye; (b) after 15 min; (c) after 30 min; (d) after 45 min.

is the initial dye concentration, and C_t is the concentration at time t. The linearity of the plot confirmed that the degradation follows pseudo-first-order kinetics. The rate constant (k) was derived from the slope and found to be 0.036 min^{-1}, with an R^2 value of 0.915, indicating a strong correlation between the model and experimental data. These kinetics imply that the degradation rate mainly depends on the dye concentration, with the catalyst's quantity remaining effectively constant throughout the process. This behavior is typical in heterogeneous catalytic degradation, where dye molecules adsorb onto the nanoparticle surface before oxidative breakdown.

3.4. Analysis of Degraded Dye Products

For the analytical characterization of degradation, an untreated Orange ME2RL dye solution was used as a control in UV–Vis, HPLC, and GC–MS analyses. This untreated dye served as a reference to compare spectral changes and identify degradation products following nanoparticle treatment.

3.4.1. FTIR of Orange ME2RL Degradation

Fig. 11 illustrates a broad band around 3410–3430 cm^{-1}, corresponding to –OH/–NH stretching vibrations, signifying hydroxylated intermediates formed during dye degradation (Silverstein et al. 2014). Peaks near 2920–2930 cm^{-1} are associated with aromatic or aliphatic C–H stretching vibrations (Stuart 2004). The gradual diminution and disappearance of the azo (–N=N–) bond vibration confirm cleavage of the dye chromophore, a key indicator of azo dye degradation (Saratale et al. 2011, Forgacs et al. 2004). The weakening of S=O and C–N stretching bands between 1200–1000 cm^{-1} further indicates the breakdown of sulfonated dye structures. The appearance of new low-frequency peaks below 700 cm^{-1} suggests the formation of low-molecular-weight inorganic or mineralized products after extended degradation (Roy et al. 2022).

3.4.2. HPLC Analysis

The HPLC chromatogram of Reactive Orange ME2RL showed distinct retention peaks. After degradation, the standard peak disappeared, and new peaks appeared at retention times of 8.572, 10.699, 13.044, 14.572, 4.017, and 16.780 min, confirming catalytic degradation of the dye (Gottlieb 2003) (Figs. 12–13).

3.4.3. GC–MS Analysis

Degradation of Orange ME2RL dye was performed using Fe_2O_3 nanoparticles. This process produced eight distinct compounds. The mass spectra of both the untreated dye and its degraded metabolites, collected at 15-minute intervals and shown in Fig. 14(a), Fig. 14(b), Fig. 14(c), and Fig. 14(d), illustrate the biodegradation pathway. During catalytic degradation, the aromatic ring of Orange ME2RL dye was cleaved, leading to the formation of several metabolites, including Sodium 6-amino-5-sulfonatonapthalen-1-yl-sulfite (1), Sodium 3-amino-7-[(4-chloro-1,3,5-triazin-2-yl) amino]-4-hydroxynaphthalene-2-sulphonate (2), Sodium 4-aminobenzene-1-sulphonate (3), Naphthalen-2-amine (4), 2-aminonaphthalen-1-ol (5), Aniline (6), Naphthalene-1-ol (7), and Benzene (8). GC–MS analysis confirmed that biosynthesized Fe_2O_3 nanoparticles serve as effective catalysts, promoting the breakdown of Orange ME2RL into low-molecular-weight compounds. The metabolites identified via GC–MS were tentatively matched with the NIST mass spectral library. The proposed degradation pathway was constructed based on these intermediates and supported by previously reported mechanisms of azo dye degradation.

3.5. Proposed Degradation Mechanism

The degradation of Reactive Orange ME2RL by *Pseudomonas*

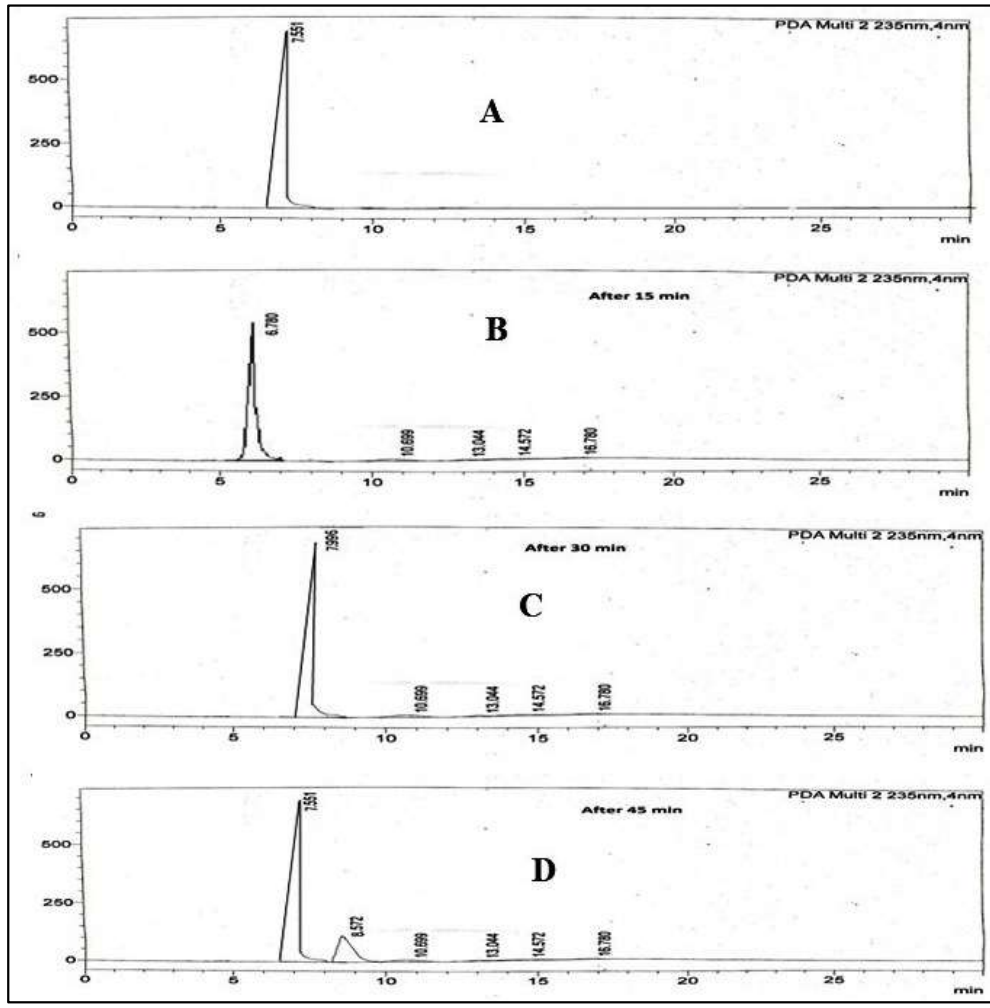

Fig. 12: HPLC chromatogram of Reactive Orange ME2RL upon degradation: (a) pure dye; (b) after 15 min; (c) after 30 min; (d) after 45 min.

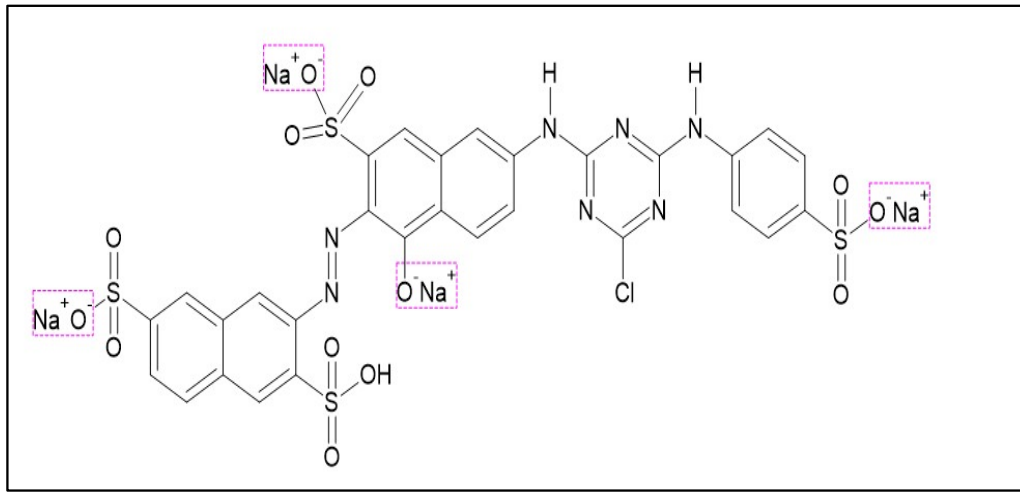

Fig. 13: Structure of the dye Reactive Orange ME2RL.

stutzeri–mediated Fe_2O_3 nanoparticles occurs through an adsorption–oxidation mechanism that differs from the pathway previously proposed for Orange ME2RL (Castro et al. 2020). The formation of intermediate ions similar to m/z 347, 390, and 159 confirms a process involving sequential azo bond cleavage, aromatic ring opening, and oxidative mineralization, as shown in Fig. 15.

3.6. Antibacterial Activity

The antibacterial efficacy of iron nanoparticles was evaluated against various pathogenic bacteria. Zones of inhibition were measured and recorded. As shown in Fig. 16 and Table 1, Fe_2O_3 NPs demonstrated notable antimicrobial activity, with inhibition zones of 25 mm for *S. aureus* NCIM-2654, 20 mm for *S. typhi* NCIM-2501, 15 mm for *P. vulgaris* NCIM-2813, and 11.66 mm for *P. aeruginosa* NCIM-5032. The reported zones of inhibition are expressed as means ± standard deviation from triplicate experiments.

Additionally, a combination of Fe nanoparticles with the antibiotic cefuroxime was tested, resulting in zones of inhibition measuring 28 mm for *S. aureus* NCIM-2654, 27 mm for *S. typhi* NCIM-2501, 26 mm for *P. vulgaris* NCIM-2813, and 25 mm for *P. aeruginosa* NCIM-5032 (Fig. 16). This combination exhibited enhanced antimicrobial activity, increasing effectiveness by 0.15, 0.16, 0.39, and 0.56 fold, respectively. The antibacterial efficacy varied between Gram-negative and Gram-positive bacteria due

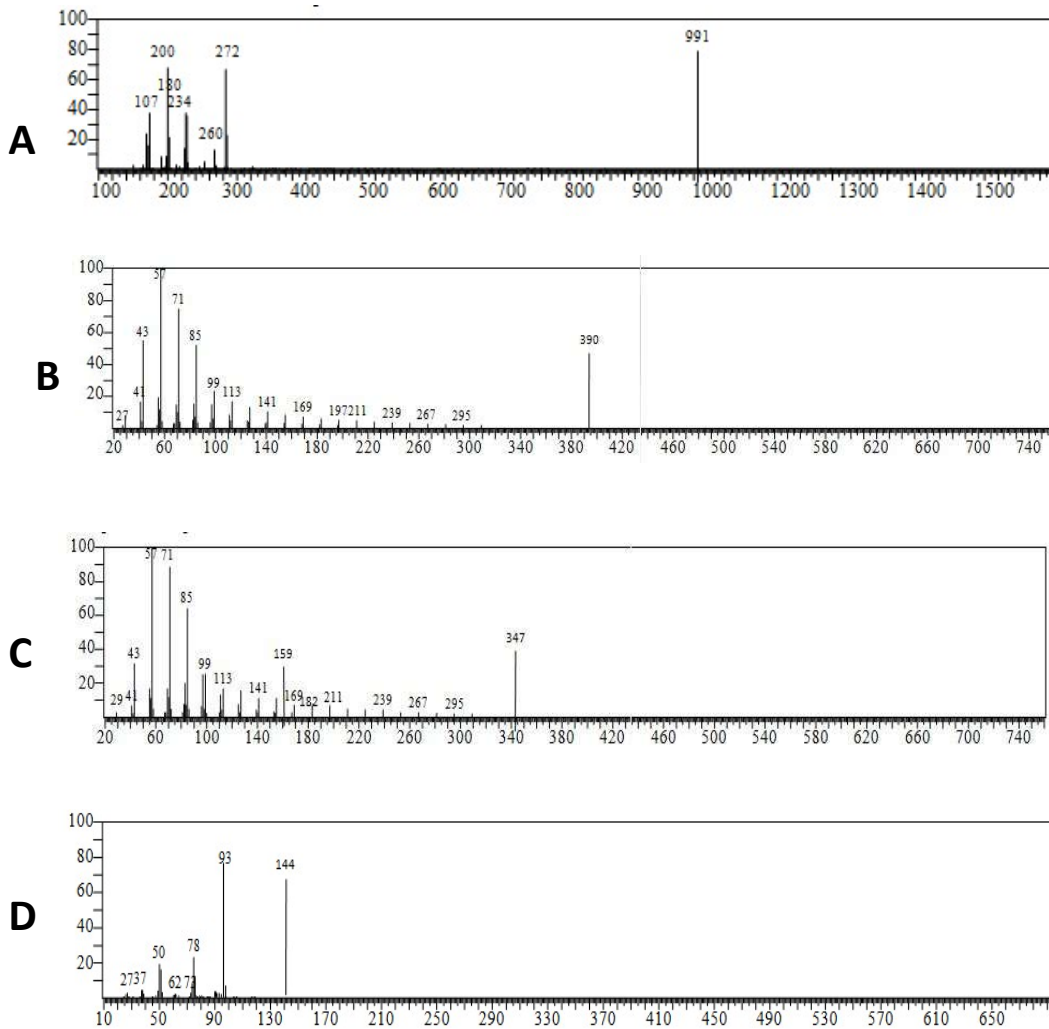

Fig. 14: GC–MS analysis of Reactive Orange ME2RL: (a) control dye (before degradation); (b) degradation after 15 min; (c) degradation after 30 min; (d) degradation after 45 min.

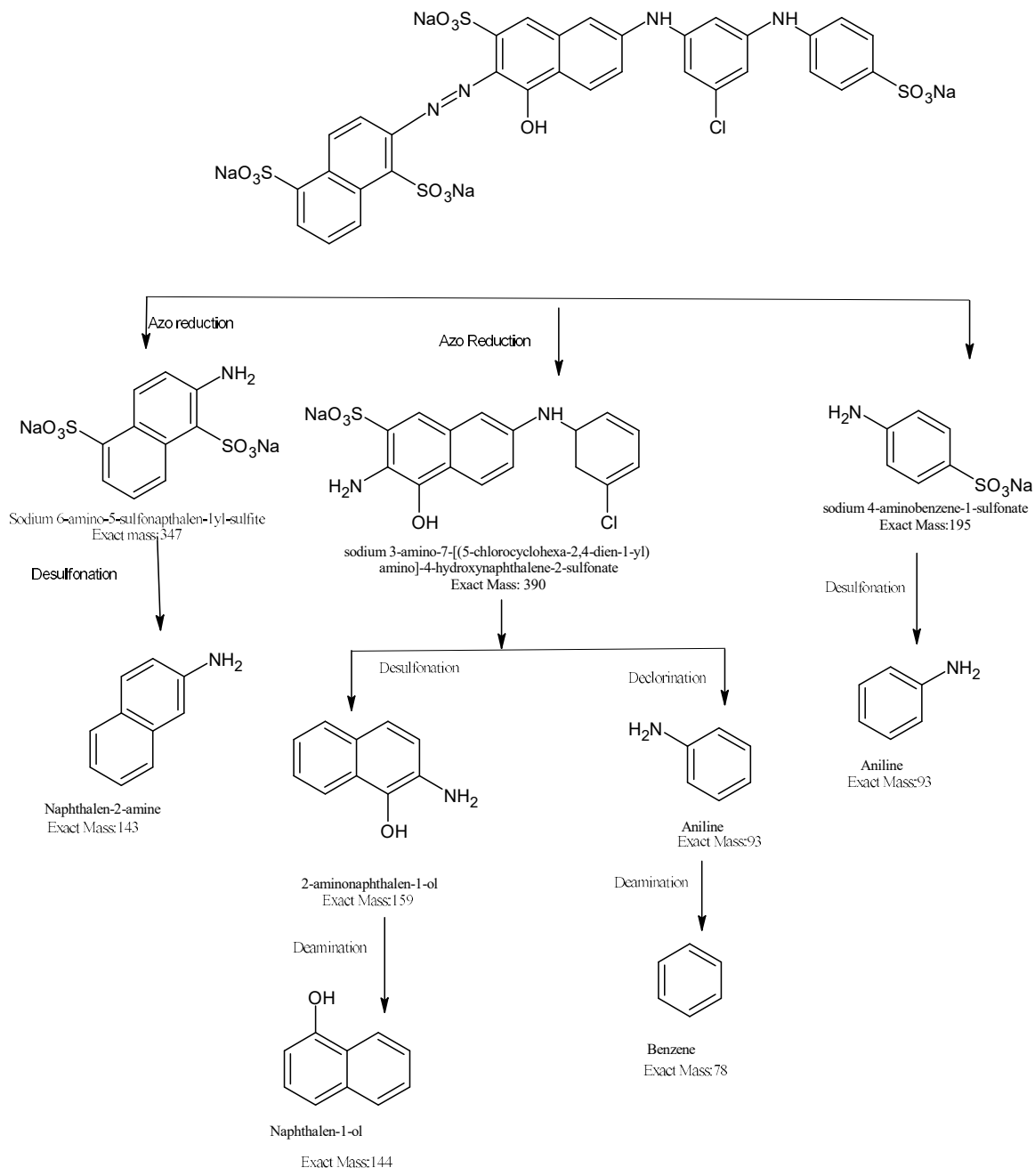

Fig. 15: Proposed degradation pathway of Reactive Orange ME2RL dye based on GC–MS analysis.

Table 1: Antibacterial activity in terms of zone of inhibition (mm) in the presence of nanoparticles and standard antibiotics.

Test organism	Diameter of zone of inhibition [mm] Nanoparticles	Std antibiotic	Std antibiotic + nanoparticles
Staphylococcus aureus	25 ± 1	27 ± 0.57	28 ± 0.57
Pseudomonas aeruginosa	11.66 ± 0.57	20.33 ± 0.57	24.66 ± 0.57
Proteus vulgaris	15 ± 2.64	21 ± 1	25.66 ± 0.57
Salmonella typhi	20.66 ± 0.57	24.66 ± 0.57	26.33 ± 1.15

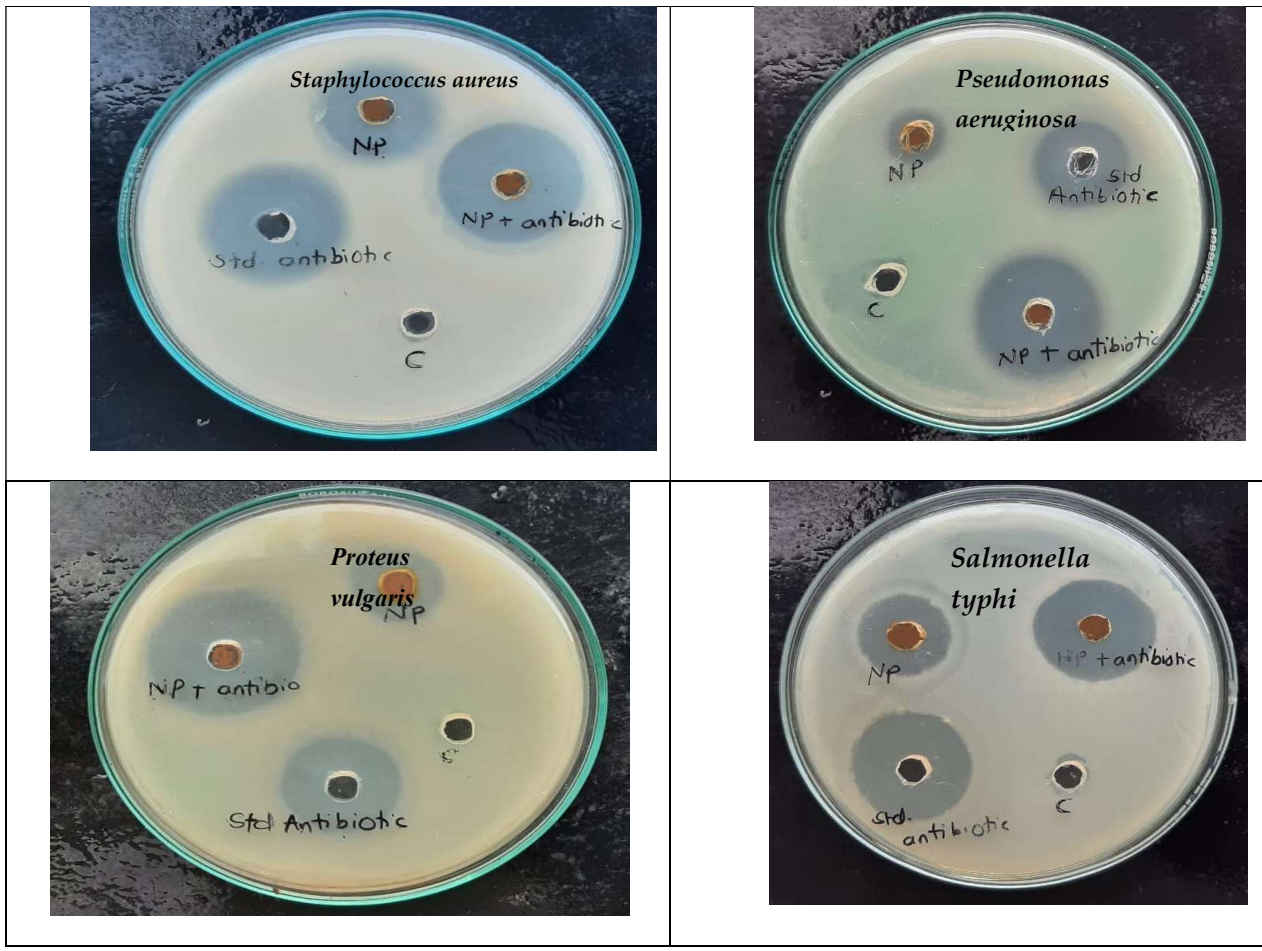

Fig. 16: Antibacterial activity of iron nanoparticles against S. aureus NCIM-2654, P. aeruginosa NCIM-5032, P. vulgaris NCIM-2813, and S. typhi NCIM-2501.

to differences in their cell wall structures (Zambare et al. 2023). Biosynthesized iron nanoparticles (Fe NPs) combat bacteria through multiple mechanisms that damage both Gram-positive and Gram-negative organisms. First, Fe NPs attach to negatively charged bacterial surfaces, disrupting membrane integrity and increasing permeability. This allows nanoparticles to enter the cells, where Fe^{2+} and Fe^{3+} ions initiate Fenton-like reactions, producing reactive oxygen species (ROS) such as hydroxyl and superoxide radicals. These ROS cause oxidative stress, damaging lipids, proteins, and DNA, leading to membrane leakage, enzyme malfunction, and genetic fragmentation. In Gram-negative bacteria, Fe NPs penetrate the outer membrane and periplasmic space, while in Gram-positive bacteria, the thick peptidoglycan layer traps the nanoparticles, sustaining ROS production. When combined with cefuroxime, Fe NPs potentiate antibiotic activity by weakening cell membranes, facilitating antibiotic entry, and impairing bacterial defence mechanisms such as efflux pumps and β-lactam enzymes. Overall, Fe_2O_3 NPs exert antibacterial effects through membrane disruption, ROS generation, interference with metal ion metabolism, and enhancement of antibiotic efficacy, showing strong potential for controlling multidrug-resistant bacteria (Hosseinzadeh 2025). Rather than a synergistic effect, Fe_2O_3 nanoparticles with standard antibiotics demonstrate an improved antibacterial effect.

3.7. Phytotoxicity

Seeds germinated in the degradation products showed significant differences compared to those germinated in Reactive Orange ME2RL, with a significance level of $P < 0.05$, as determined by the Tukey–Kramer multiple comparison test. The degradation of dyes does not always produce benign by-products; instead, it may generate compounds that are more harmful than the parent dye. Previous studies demonstrated that the treatment of azo dyes could result in the formation of aromatic amines that are more toxic than the original dyes (Gottlieb et al. 2003).

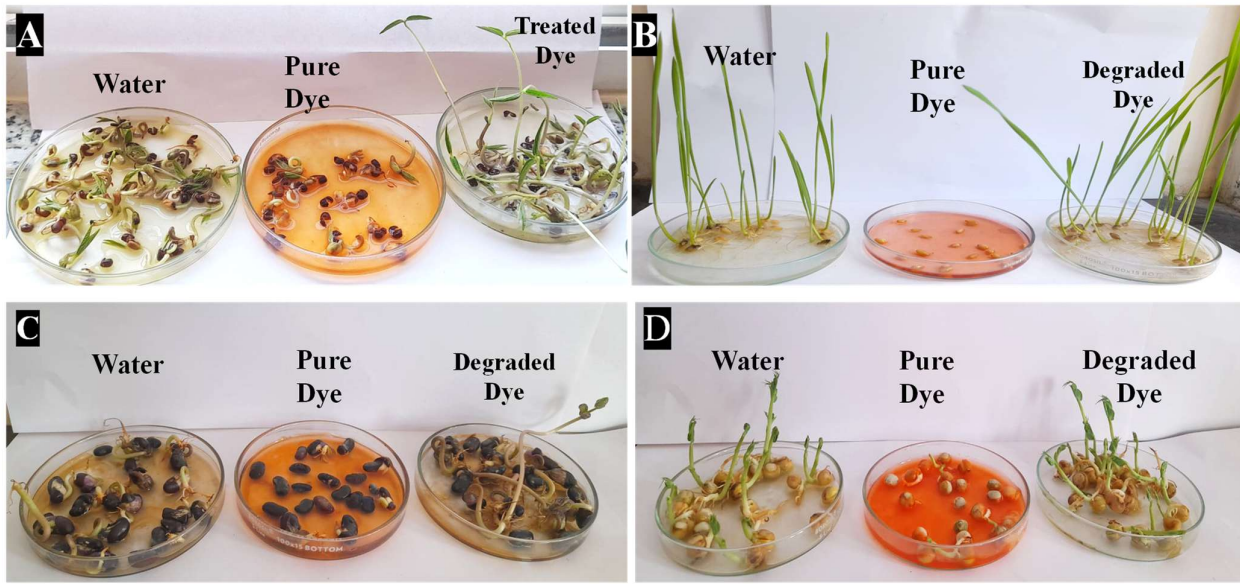

Fig. 17: Phytotoxicity analysis of pure dye Reactive Orange ME2RL and its metabolites using seeds: (a) green gram; (b) Triticum aestivum; (c) Vigna unguiculata; (d) Pisum sativum.

Consequently, a phytotoxicity assessment was undertaken to evaluate the potential harmful effects of the degraded metabolites on the seeds of green gram, *Triticum aestivum*, *Vigna unguiculata*, and *Pisum sativum*. All seeds were exposed to Reactive Orange ME2RL and its degraded metabolites at a concentration of 100 ppm.

The findings, presented in Table 2 and Fig. 17, showed the germination rate, as well as the radicle and plumule lengths, across all plant species tested. The degraded metabolites resulted in a notable increase in both root and shoot lengths in all plant species. In contrast, the untreated dye produced significantly lower seed germination rates and stunted root and shoot growth in all four plant species compared to the degraded metabolites. Based on these results, it appears that the degradation products not only eliminated toxicity but also promoted seed growth (Survase & Kanase 2022).

Table 2: Phytotoxicity analysis of pure dye Reactive Orange ME2RL and its metabolites using seeds of green gram, *Triticum aestivum*, *Vigna unguiculata*, and *Pisum sativum*.

Parameters studied	Water	Orange ME2RL	Degraded metabolites
Vigna radiata			
Radicle [cm]	2.1 ± 0.1	1.16 ± 0.057	2.5 ± 0.1
Plumule [cm]	4.13 ± 0.11	0.23 ± 0.1	10.33 ± 0.57
Germination [%]	100	28.33 ± 2.88	100
Triticum aestivum			
Radicle [cm]	1.86 ± 0.057	0.16 ± 0.057	3.1 ± 0.1
Plumule [cm]	9.1 ± 0.1	0.23 ± 0.057	12.1 ± 0.1
Germination [%]	100	5	100
Vigna unguiculata			
Radicle [cm]	14.1 ± 0.1	0.13 ± 0.057	8.03 ± 0.20
Plumule [cm]	12.1 ± 0.1	0.26 ± 0.057	10.5 ± 0.1
Germination [%]	100	20	100
Pisum sativum			
Radicle [cm]	3.9 ± 0.1	0.13 ± 0.057	3.76 ± 0.05
Plumule [cm]	4.46 ± 0.057	2.5 ± 0.1	4.86 ± 0.05
Germination [%]	100	30	100

The improved growth parameters observed in *Vigna radiata* treated with the degraded dye metabolites, compared with the water control, may indicate not only detoxification but also possible nutrient enrichment effects. During the degradation process, complex dye molecules are broken down into smaller organic intermediates and inorganic ions, which may serve as additional nutrient sources for plant growth. These metabolites may enhance seed germination and seedling development by providing readily available carbon or nitrogen sources.

3.8. Fish Toxicity

To determine the lethal concentration of pure dye, fish were exposed to different concentrations of pure dye for 24, 48, 72, and 96 h. The percent mortality for pure dye at 96 h was calculated as shown in Table 3.

The acute toxicity test showed that fish mortality increased with increasing concentrations of the test sample. No mortality was observed at 1.25 ppm after 96 h of exposure, whereas complete mortality (100%) occurred at 8.75 ppm (Table 3). Approximately 50% mortality was observed at 5 ppm, indicating that the 96 h LC_{50} value was close to this concentration.

The observed LC_{50} value was 5 ppm (5 µL L^{-1}), whereas the statistically calculated LC_{50} value obtained from probit analysis was 4.8 ppm ($\approx$4.5 µL L^{-1}). The close agreement between the observed and calculated LC_{50} values indicates good consistency and reliability of the experimental data.

Table 3: Effect of Orange ME2RL on mortality of Cirrhinus mrigala during a 96 h exposure period.

No. of fishes	Concentration [ppm]	Exposure period [h]				% mortality
		24	48	72	96	
10	1.25	0	0	0	0	0
10	2.50	0	0	0	1	10
10	3.75	0	0	1	2	30
10	**5.00**	**0**	**1**	**2**	**2**	**50**
10	6.25	1	1	2	3	70
10	7.5	1	2	3	3	90
10	8.75	6	4	-	-	100

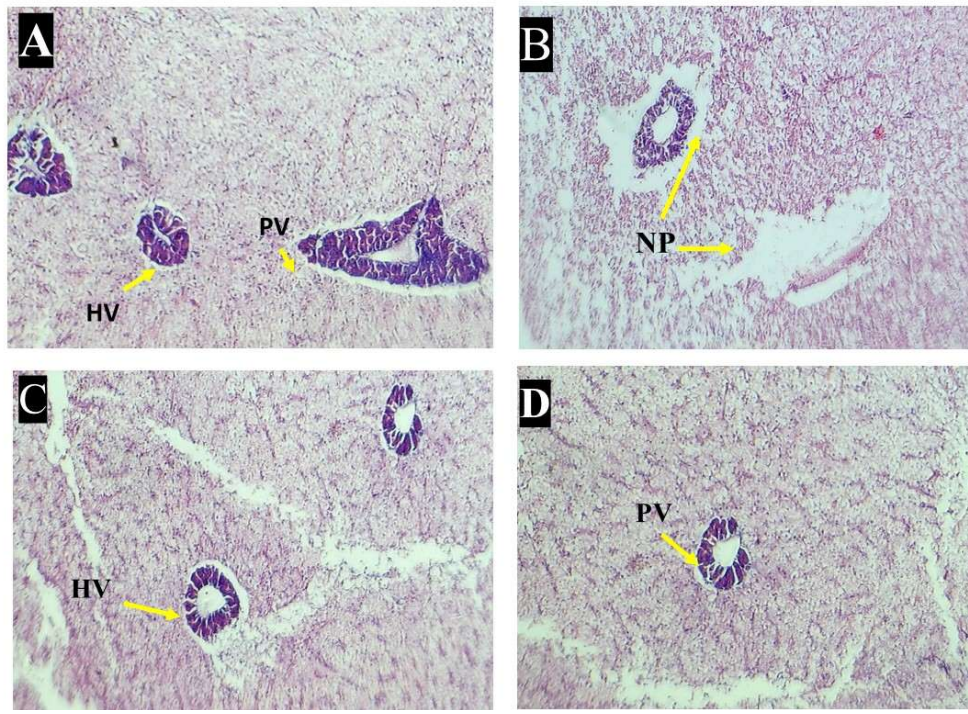

Fig. 18: Histopathological changes in the liver: (a) freshwater control; (b) exposure to pure dye; (c) exposure to treated dye; (d) exposure to nanoparticles.

These results suggest that the test compound exhibits significant toxic effects on fish even at relatively low concentrations.

3.8.1. Histological Observations of Liver

The histological structure of the liver in control fish is depicted in the photomicrograph in Fig. 18. These H&E-stained liver slices reveal hepatic cells situated within the bile canaliculi network. The hepatic cells feature spherical, blue-stained nuclei located centrally, with a morphology ranging from round to polygonal. Glycogen granules are plentiful within these cells. The hepatic cell cords, which form cord-like structures surrounding the sinusoids, are not distinct; each cord contains a centrally positioned bile canaliculus. Hepatocytes are oriented with their bases facing the sinusoids and their apices directed toward the wall of the bile canaliculi. The arrangement of blood vessels and the bile duct appears irregular, and there is no clear separation of hepatic cells within the lobules. Lipid droplets are observed inside rounded or elongated Ito (fat-storing) cells. Kupffer cells are occasionally seen lining the sinusoids, containing a significant amount of cytoplasm. The portal vein is present, surrounded by pancreatic acini, collectively forming the hepatopancreas. The hepatic arteries have narrow lumens enclosed by a dense layer of endothelial cells. Within each hepatic lobule, an intralobular central vein can be seen, containing blood cells in its lumen.

The liver is a primary target for toxicants due to its extensive blood supply. Numerous toxicants have been studied for their harmful effects on the liver, as it is considered the main organ for bioaccumulation (van Dyk et al. 2007). When fish were exposed to a pure dye, significant degenerative changes were observed in their livers compared to the control group (Fig. 18). These histological alterations included disorganization of hepatic cords, widespread dilation of sinusoids throughout the tissue, and increased sinusoidal spaces around the portal vein. There was also complete degeneration of hepatocytes with severe necrotic patches, along with cytoplasmic degeneration, vacuolation within hepatocytes, and evidence of karyolysis. Some regions showed elongation of blood vessels, and the hepatopancreas exhibited degeneration.

Fig. 18(c) and Fig. 18(d) depict the treated dye and the liver alterations induced by exposure to nanoparticles. Mild degenerative changes were observed in fish exposed to the nanoparticles, although these changes were less pronounced than those observed in the control group. These alterations included disorganization of the hepatic cords, the onset of sinusoidal space expansion, cytoplasmic vacuolation, cellular swelling, and pyknotic nuclei in some cells. Although mild degeneration was observed, no significant alterations were detected in the livers of fish exposed to the nanoparticles compared with those exposed to the pure dye.

3.8.2. Histological Observations of Gills

The histological structure of the gills in *Cirrhinus mrigala* closely resembles that of most freshwater teleosts. An operculum protects each gill, and there are four pairs of gills. These gills are supported by curved bony gill arches covered with multilayered epithelium. Each gill arch bears two rows of primary gill lamellae, which are located on one side only. These lamellae are wider at the base and taper toward the tip. They consist of a central vascular core surrounded by a wall made of three to four epithelial layers, with connective tissue interposed. The primary gill lamellae rest on a central cartilaginous matrix that encompasses chondrocytes. The epithelial cells at the tips of the lamellae are mainly oval to flat, with centrally located nuclei and basophilic, homogeneous cytoplasm.

Additionally, each primary gill lamella features two rows of delicate filamentous structures known as secondary gill lamellae or secondary gill filaments (Fig. 19(a)), oriented perpendicular to the primary lamellae's axis. These secondary lamellae develop as outward extensions from the primary lamellae and are composed of a single layer of epithelial cells, which are oval to cuboidal, with basophilic cytoplasm and centrally located oval nuclei. Internally, the secondary lamellae contain a central core of blood sinuses lined by large oval to rounded pillar cells. These pillar cells have homogeneous, basophilic cytoplasm and round nuclei positioned centrally.

Following 96 h of exposure to pure dye, degenerative alterations were noted in the gill structure. Tilting and congestion were observed at the tips of the primary gill lamellae (refer to Fig. 19(b)). Additionally, detachment of the epithelium from the central supporting material of the primary gill lamellae was evident. Significant enlargement of the central supporting material of the primary gill lamellae was also observed. Furthermore, progressive hyperplasia and thickening of the epithelium at the interlamellar region were observed. Shortening and fusion of adjacent secondary gill lamellae were noted in a certain region, as shown in Fig. 19b.

Mild histopathological changes were observed in the gills after exposure to degraded dye, as shown in Fig. 19(c). A slight enlargement of the tips of the primary gill lamellae was noted, with these dilated tips filled with blood cells. An increased number of mucous cells, particularly at the tips of the primary gill lamellae, was also observed (Fig. 19(c)). Additionally, the secondary gill lamellae appeared curved with dilated tips filled with blood cells. There was slight desquamation of the epithelial lining from the

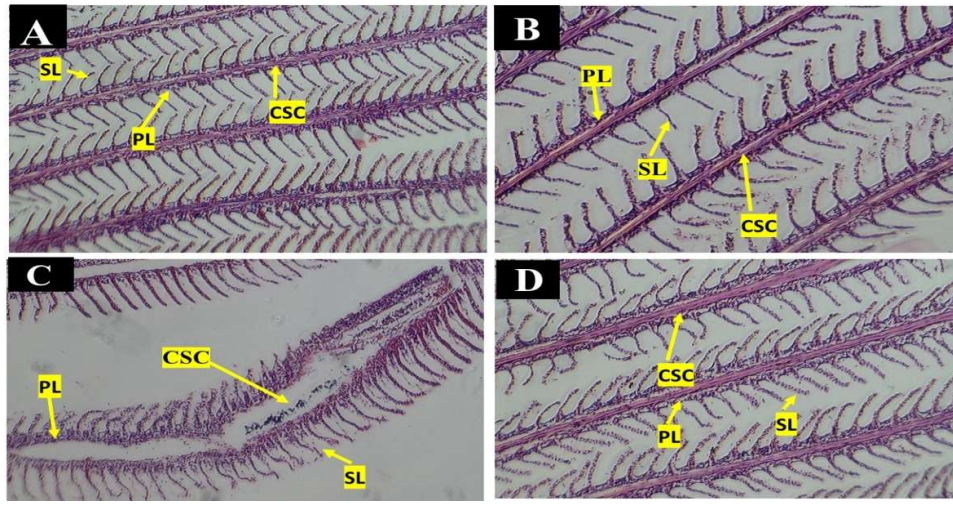

Fig. 19: Histopathological changes in the gills: (a) freshwater control; (b) exposure to pure dye; (c) exposure to treated dye; (d) exposure to nanoparticles.

central supporting cartilage upon exposure to nanoparticles (Fig. 19(d)). These changes were less pronounced than those seen following exposure to pure dye.

4. CONCLUSIONS

This study presents the eco-friendly biosynthesis of Fe_2O_3 nanoparticles using *Pseudomonas stutzeri*. Characterization by UV–Visible spectroscopy, SEM, FTIR, XRD, HRTEM, and DLS confirmed the formation of predominantly spherical nanoparticles with sizes ranging from 30 to 50 nm. The nanoparticles demonstrated strong catalytic activity in degrading Reactive Orange ME2RL dye, and the degradation metabolites were identified using FTIR, HPLC, and GC–MS analyses. They also exhibited antibacterial activity against *Staphylococcus aureus*, *Salmonella typhi*, *Proteus vulgaris*, and *Pseudomonas aeruginosa*, with greater inhibition observed when combined with antibiotics. Phytotoxicity and fish toxicity assays revealed that the degraded dye products were less toxic than the original dye. The synthesized Fe_2O_3 nanoparticles showed high degradation efficiency towards Reactive Orange ME2RL, indicating their suitability for the treatment of dye-containing industrial effluents. Fe_2O_3 nanoparticles possess inherent magnetic properties that enable the easy separation and potential reuse of the catalyst from treated wastewater using an external magnetic field. Therefore, this study provides a sustainable and efficient approach for the remediation of textile dye pollutants and demonstrates potential applicability in large-scale industrial wastewater treatment processes. Further studies are required to evaluate the reusability and long-term stability of the synthesized Fe_2O_3 nanoparticles over multiple degradation cycles to assess their practical applicability in wastewater treatment. Owing to the magnetic nature of Fe_2O_3 nanoparticles, their recovery and reuse may be feasible and will be explored in future studies.

5. ACKNOWLEDGMENTS

The authors are grateful to the Rayat Institute of Research and Development, Satara, for providing the prestigious Dr. B.M. Sawant fellowship and laboratory facilities as financial provision for the research endeavour.

5. REFERENCES

Acharya, C., Mishra, S., Chaurasia, S.K., Pandey, B.K., Dhar, R. and Pandey, J.K., 2025. Synthesis of metallic nanoparticles using biometabolites: mechanisms and applications. In: *BioMetals*, Vol. 38(1). Springer, Cham, Switzerland, pp. 21–54. [DOI]

Ali, H., 2010. Biodegradation of synthetic dyes: a review. *Water, Air, and Soil Pollution*, 213(1-4), pp. 251-273. [DOI]

Al-Musawi, T.J., McKay, G., Rajiv, P., Mengelizadeh, N. and Balarak, D., 2022. Sonophotocatalytic degradation of Acid Blue 113 using $CoFe_2O_4$-MWCNT nanocomposite. *Journal of Photochemistry and Photobiology A: Chemistry*, 424, p. 113617. [DOI]

Aly, H. and Abdelsalam, A., 2025. Effect of humic acid and selenium on seed germination, seedling growth, and priming with mitigate salt stress effect on mustard (Brassica juncea) seeds. *Russian Journal of Plant Physiology*, *72*(3), p.72. [DOI]

Ameur, W.B., de Lapuente, J., El Megdiche, Y., Barhoumi, B., Trabelsi, S., Camps, L. and Borràs, M., 2012. Oxidative stress, genotoxicity and histological effects in fish from Bizerte lagoon. *Marine Pollution Bulletin*, 64(2), pp. 241-251. [DOI]

Annamalai, J., Ummalyma, S.B., Pandey, A. and Bhaskar, T., 2021. Recent trends in microbial nanoparticle synthesis and potential application in environmental technology: a comprehensive review. *Environmental Science and Pollution Research*, *28*(36), pp.49362-49382 [DOI]

Apine, O., Patil, S., Patil, D. and Jadhav, J.P., 2023. Role of analytical techniques in treatment of synthetic dyes and textile effluent. In: Pandey, A. et al. (eds) *Current Developments in Bioengineering and Biotechnology*. Elsevier: Amsterdam, Netherlands, pp. 303–338. [DOI]

Banat, I.M., Nigam, P., Singh, D. and Marchant, R., 1997. Microbial decolorization of textile-dye-containing effluents: a review. *Bioresource Technology*, 61(1), pp. 103-115. [DOI]

Bhattacharjee, S., 2016. DLS and zeta potential–what they are and what they are not? *Journal of Controlled Release*, 235, pp. 337-351. [DOI]

Castro, L., Meurer, E., Alves, H., Santos, M., Vasques, E. and Colpini, L., 2020. Photocatalytic degradation of Orange-122 via electrospray MS. *Brazilian Archives of Biology and Technology*, 63, p. e20180573. [DOI]

Chavan, R.B., 2001. Indian textile industry—environmental issues. *Indian Journal of Fibre and Textile Research*, 26(1–2), pp. 11–21.

Chicea, D., Indrea, E. and Cretu, C.M., 2012. Assessing Fe_3O_4 nanoparticle size by DLS, XRD and AFM. *Journal of Optoelectronics and Advanced Materials*, 14(5), pp. 460–466.

Ferreira, F.N., Benevides, A.P., Cesar, D.V., Luna, A.S. and de Gois, J.S., 2020. Magnetic solid-phase extraction of estrogenic compounds using maghemite–graphene oxide nanoparticles. *Microchemical Journal*, 157, p. 104947. [DOI]

Forgacs, E., Cserháti, T. and Oros, G., 2004. Removal of synthetic dyes from wastewaters: a review. *Environment International*, 30(7), pp. 953–971. [DOI]

Ganachari, S.V., Joshi, V., Bhat, R., Deshpande, R., Salimath, B., Rao, N.V. and Venkataraman, A., 2012. Large scale synthesis and characterization of γ-Fe_2O_3 nanoparticles by self-propagating low temperature combustion method. *International Journal of Science Research*, 1(2), pp. 77–79.

Giuli, G., Trapananti, A., Mueller, F., Bresser, D., d'Acapito, F. and Passerini, S., 2015. Effects of Fe and Co doping on nanosized ZnO structure. *Inorganic Chemistry*, 54(19), pp. 9393–9400. [DOI]

Gottlieb, A.L., 2003. *Microbial Degradation of Textile Dyes to Safe End-Products*. Doctoral Thesis. Nottingham Trent University: Nottingham, UK, pp. 1–180.

Gottlieb, A., Shaw, C., Smith, A., Wheatley, A. and Forsythe, S., 2003. Toxicity of textile azo dyes after hydrolysis and decolourization. *Journal of Biotechnology*, 101, pp. 49–56. [DOI]

Gupta, V.K., Mittal, A., Gajbe, V. and Mittal, J., 2006. Removal and recovery of the hazardous azo dye acid orange 7 through adsorption over waste materials: bottom ash and de-oiled soya. *Industrial & Engineering Chemistry Research*, 45(4), pp. 1446–1453. [DOI]

Hanafi, M.F. and Sapawe, N., 2020. A review on the current techniques and technologies of organic pollutants removal from water/wastewater. *Materials Today: Proceedings*, *31*, pp. A158–A165. [DOI]

Haroon, K., Kherb, J., Jeyaseelan, C. and Sen, M.J.N.E., 2023. Recent advances and sustainable approaches towards efficient wastewater treatment using natural waste derived nanocomposites: a review. *Nature Environment & Pollution Technology*, 22(3), pp. 1251–1264. [DOI]

Holzwarth, U. and Gibson, N., 2011. The Scherrer equation versus the Debye–Scherrer equation. *Nature Nanotechnology*, 6(9), pp. 534–535. [DOI]

Hosseinzadeh, H., 2025. Antibacterial/magnetic iron oxide nanoparticles: synthesis, doping and applications. *Journal of Applied Material Science*, 1(3), p. e210146.

Islam, M.A., Amin, S.N., Brown, C.L., Juraimi, A.S., Uddin, M.K. and Arshad, A., 2021. LC50 of pesticides and histopathology in African catfish. *Toxics*, 9(12), p. 340. [DOI]

Jana, J., Ganguly, M. and Pal, T., 2016. Surface plasmon resonance of metal nanoparticles for spectroscopic applications. *RSC Advances*, 6(89), pp. 86174–86211. [DOI]

Javidparvar, A.A., Ramezanzadeh, B. and Ghasemi, E., 2016. Effect of surface treatment of Fe_3O_4 nanoparticles on epoxy coating corrosion resistance. *Journal of the Taiwan Institute of Chemical Engineers*, 61, pp. 356–366. [DOI]

Joshi, A., Nanani, J., Trivedi, N., Kothari, V. and Kothari, R., 2015. Decolorization of Reactive Orange Me2RL by bacterial consortium. *National Science Symposium Proceedings*, 2, p. 164.

Joshi, A.U., Hinsu, A.T., Kotadiya, R.J., Rank, J.K., Andharia, K.N. and Kothari, R.K., 2020. Decolorization and biodegradation of textile di-azo dye Acid Blue 113 by Pseudomonas stutzeri AK6. *3 Biotech*, 10(5), p. 214. [DOI]

Katata-Seru, L., Moremedi, T., Aremu, O.S. and Bahadur, I., 2018. Green synthesis of iron nanoparticles using Moringa oleifera extracts. *Journal of Molecular Liquids*, 256, pp. 296–304. [DOI]

Khan, I., Saeed, K. and Khan, I., 2019. Nanoparticles: properties, applications and toxicities. *Arabian Journal of Chemistry*, 12(7), pp. 908–931. [DOI]

Mane, U.V., Gurav, P.N., Deshmukh, A.M. and Govindwar, S.P., 2008. Degradation of textile dye Reactive Blue 59 by Streptomyces krainskii SUK-5. *Malaysian Journal of Microbiology*, 4(2), pp. 1–5. [DOI]

Mukherjee, B. and Dutta, S., 2019. Isolation of a phosphate-solubilizing bacterial strain Bacillus tequilensis MCC 3872 from rice field and characterization of its plant growth-promoting traits. *Pharma Innovation Journal*, 8, pp. 956–962.

Naz, M., Rafiq, A., Ikram, M., Haider, A., Ahmad, S.O., Haider, J. and Naz, S., 2021. Elimination of dyes by catalytic reduction in the absence of light: a review. *Journal of Materials Science*, 56(28), pp. 15572–15608. [DOI]

Nurbas, M.A., Ghorbanpoor, H.A. and Avci, H.Ü., 2017. Eco-friendly synthesis of magnetite (Fe_3O_4) nanoparticles using Platanus orientalis leaf extract. *Digest Journal of Nanomaterials and Biostructures*, 12(4), pp. 1231–1240.

Palleroni, N.J., 1984. Pseudomonas. In: Krieg, N.R. (ed.) *Bergey's Manual of Systematic Bacteriology*, Vol. I. Williams and Wilkins: Baltimore, United States, pp. 141–199.

Palleroni, N.J., Doudoroff, M., Stanier, R.Y., Solanes, R.E. and Mandel, M., 1970. Taxonomy of the aerobic pseudomonads: the properties of the Pseudomonas stutzeri group. *Microbiology*, 60(2), pp. 215–231. [DOI]

Palleroni, N.J., Kunisawa, R., Contopoulou, R. and Doudoroff, M., 1973. Nucleic acid homologies in the genus Pseudomonas. *International Journal of Systematic Bacteriology*, 23, pp. 333–339. [DOI]

Pandey, A., Singh, P. and Iyengar, L., 2007. Bacterial decolorization and degradation of azo dyes. *International Biodeterioration and Biodegradation*, 59(2), pp. 73–84. [DOI]

Patel, D.D. and Bhatt, S., 2022. Environmental pollution, toxicity profile, and physico-chemical and biotechnological approaches for treatment of textile wastewater. *Biotechnology and Genetic Engineering Reviews*, 38(1), pp. 33–86. [DOI]

Periyasamy, A.P., 2024. Recent advances in the remediation of textile-dye-containing wastewater: prioritizing human health and sustainable wastewater treatment. *Sustainability*, 16(2), p. 495. [DOI]

Rossello, R., Garcia-Valdes, E., Lalucat, J. and Ursing, J., 1991. Genotypic and phenotypic diversity of Pseudomonas stutzeri. *Systematic and Applied Microbiology*, 14(2), pp. 150–157. [DOI]

Roy, A., Khan, A., Ahmad, I., Alghamdi, S., Rajab, B.S., Babalghith, A.O., Alshahrani, M.Y., Islam, S. and Islam, M.R., 2022. Flavonoids a bioactive compound from medicinal plants and its therapeutic applications. *BioMed Research International*, *2022*(1), p.5445291. [DOI]

Saha, S. and Bhunia, A.K., 2020. Synthesis of Fe_2O_3 nanoparticles and study of structural and optical properties. *Materials Today: Proceedings*, pp. 1–8. [DOI]

Saratale, R.G., Saratale, G.D., Chang, J.S. and Govindwar, S.P., 2011. Bacterial decolorization and degradation of azo dyes: a review. *Journal of the Taiwan Institute of Chemical Engineers*, *42*(1), pp.138-157. [DOI]

Sekar, S., Surianarayanan, M., Ranganathan, V., MacFarlane, D. and Mandal, A., 2012. Choline-based ionic liquids enhance biodegradation of azo dyes. *Environmental Science and Technology*, 46(9), pp. 4902–4908. [DOI]

Shahriarinour, M., Divsar, F., Dahka, F.K., Chegini, S.N., Mahani, M., Moeini, A. and Cerruti, P., 2021. Biodegradation of alprazolam in

pharmaceutical wastewater using mesoporous nanoparticle-adhered Pseudomonas stutzeri. *Molecules*, 27(1), p. 237. [DOI]

Shakoor, S., Khan, M.S. and Khan, M.E., 2025. Adsorptive remediation of dyes through a novel approach from nanotechnology: A comprehensive review. *Nature Environment and Pollution Technology*, 24(1), pp. 1-15. [DOI]

Silverstein, M.S., 2014. PolyHIPEs: recent advances in emulsion-templated porous polymers. *Progress in Polymer Science*, *39*(1), pp.199-234. [DOI]

Srivastava, S.K. and Constanti, M., 2012. Room-temperature biogenic synthesis of multiple nanoparticles by Pseudomonas aeruginosa SM1. *Journal of Nanoparticle Research*, 14, pp. 1–10. [DOI]

Stuart, B.H., 2004. *Infrared Spectroscopy: Fundamentals and Applications*.

Survase, A. and Kanase, S., 2022. Green synthesis of TiO_2 nanospheres by Aspergillus eucalypticola SLF1 and dye degradation. *Ceramics International*, 49(10), pp. 14964–14980. [DOI]

Van Dyk, J.C., Pieterse, G.M. and van Vuren, J.H.J., 2007. Histological changes in liver of Oreochromis mossambicus after cadmium and zinc exposure. *Ecotoxicology and Environmental Safety*, 66, pp. 432–440. [DOI]

Vasantharaj, S., Sathiyavimal, S., Senthilkumar, P., Lewis-Oscar, F. and Pugazhendhi, A., 2019. Biosynthesis of iron oxide nanoparticles using leaf extract of Ruellia tuberosa. *Journal of Photochemistry and Photobiology B: Biology*, 192, pp. 74–82. [DOI]

Velusamy, P., Kumar, G.V., Jeyanthi, V., Das, J. and Pachaiappan, R., 2016. Bio-inspired green nanoparticles: synthesis, mechanism and antibacterial application. *Toxicological Research*, 32, p. 95. [DOI]

Vu, X.H., Phuoc, L.H., Dien, N.D., Pham, T.T.H. and Thanh, L.D., 2019. Photocatalytic degradation of Methylene Blue (MB) over α-Fe_2O_3 nanospindles prepared by a hydrothermal route. *Journal of Electronic Materials*, 48, pp. 2978–2985. [DOI]

Huang, Y., Ding, D., Zhu, M., Meng, W., Huang, Y., Geng, F., Li, J., Lin, J., Tang, C. and Lei, Z., 2015. Facile synthesis of α-Fe_2O_3 nanodisk with superior photocatalytic performance and mechanism insight. *Science and Technology of Advanced Materials*, 16, p. 014801. [DOI]

Wu, K., Shi, M., Pan, X., Zhang, J., Zhang, X., Shen, T. and Tian, Y., 2022. Decolorization and biodegradation of methylene blue dye by ligninolytic enzyme-producing Bacillus thuringiensis. *Enzyme and Microbial Technology*, 156, p. 109999. [DOI]

Zambare, P., Survase, A. and Kanase, S., 2023. Green synthesis of copper nanoparticles using leaf extract of Ocimum sanctum and its antimicrobial activity. *International Journal of Pharmaceutical Investigation*, 13(1), pp. 106–112. [DOI]

Zhao, H., Huang, M., Wu, J., Wang, L. and He, H., 2016. Preparation of Fe_3O_4@PPy magnetic nanoparticles for preconcentration of phthalates. *Journal of Chromatography B*, 1011, pp. 33–44. [DOI]